Lawrence Berkeley National Laboratory
LBL Publications

Title
Signatures of Weyl Fermion Annihilation in a Correlated Kagome Magnet

Authors
Belopolski, Ilya
Cochran, Tyler A
Liu, Xiaoxiong
et al.

Peer reviewed

Signatures of Weyl fermion annihilation
in a correlated kagome magnet

Ilya Belopolski*,[1,2,†] Tyler A. Cochran*,[1] Xiaoxiong Liu*,[3] Zi-Jia Cheng*,[1]
Xian P. Yang,[1] Zurab Guguchia,[1,4] Stepan S. Tsirkin,[3] Jia-Xin Yin,[1] Praveen
Vir,[5] Gohil S. Thakur,[5,6] Songtian S. Zhang,[1] Junyi Zhang,[7] Konstantine
Kaznatcheev,[8] Guangming Cheng,[9] Guoqing Chang,[10] Daniel Multer,[1] Nana
Shumiya,[1] Maksim Litskevich,[1] Elio Vescovo,[8] Timur K. Kim,[11] Cephise
Cacho,[11] Nan Yao,[9] Claudia Felser,[5] Titus Neupert,[3] and M. Zahid Hasan[1,9,12,‡]

[1] *Laboratory for Topological Quantum Matter and Spectroscopy (B7),*
Department of Physics, Princeton University,
Princeton, New Jersey 08544, USA

[2] *RIKEN Center for Emergent Matter Science (CEMS), Wako, Saitama 351-0198, Japan*

[3] *Department of Physics, University of Zurich,*
Winterthurerstrasse 190, 8057 Zurich, Switzerland

[4] *Laboratory for Muon Spin Spectroscopy,*
Paul Scherrer Institute, Villigen PSI, Switzerland

[5] *Max Planck Institute for Chemical Physics of Solids,*
Nöthnitzer Straße 40, 01187 Dresden, Germany

[6] *Faculty of Chemistry and Food Chemistry,*
Technische Universitat, 01069 Dresden, Germany

[7] *Department of Physics, Princeton University,*
Princeton, New Jersey 08544, USA

[8] *National Synchrotron Light Source II,*
Brookhaven National Laboratory, Upton, New York 11973, USA

[9] *Princeton Institute for Science and Technology of Materials,*
Princeton University, Princeton, New Jersey, 08544, USA

[10] *Division of Physics and Applied Physics,*
School of Physical and Mathematical Sciences,
Nanyang Technological University, 21 Nanyang Link, 637371, Singapore

---

* These authors contributed equally to this work.

arXiv:2105.14034v2 [cond-mat.str-el] 18 Jan 2022

^{11}*Diamond Light Source, Didcot OX11 0DE, UK*

^{12}*Materials Sciences Division, Lawrence Berkeley*

National Laboratory, Berkeley, CA 94720, USA

(Dated: January 20, 2022)

Abstract

The manipulation of topological states in quantum matter is an essential pursuit of fundamental physics and next-generation quantum technology. Here we report the magnetic manipulation of Weyl fermions in the kagome spin-orbit semimetal $Co_3Sn_2S_2$, observed by high-resolution photoemission spectroscopy. We demonstrate the exchange collapse of spin-orbit-gapped ferromagnetic Weyl loops into paramagnetic Dirac loops under suppression of the magnetic order. We further observe that topological Fermi arcs disappear in the paramagnetic phase, suggesting the annihilation of exchange-split Weyl points. Our findings indicate that magnetic exchange collapse naturally drives Weyl fermion annihilation, opening new opportunities for engineering topology under correlated order parameters.

Quantum magnets exhibiting electronic topology are attracting considerable interest for the magnetic manipulation of Weyl and Dirac quasiparticles, as well as their topological surface states [1–7]. To date, spectroscopic signatures of electronic topological ground states have been observed in several magnetic semimetals, comprising magnetic Weyl loops [8]; Weyl points [9–13]; and massive Dirac fermions [14]. In parallel, the magnetic manipulation of Weyl and Dirac fermions has been extensively explored in transport [15–20]. However, direct spectroscopic observation of magnetic control of topology remains challenging. Demonstrating coherent evolution of topological quasiparticles under varying magnetic order, such as the annihilation of Weyl points, offers the possibility to directly verify fundamental notions of topological band theory [2, 3, 21, 22]. Furthermore, novel transport and optical effects are enabled by tuning the relative energies of Weyl loops and points [23–25], controlling their positions relative to the Fermi level [8, 26–29] and switching on/off their topological surface states [30, 31].

We have investigated magnetic modulation of topological semimetallic states in a range of materials by spectroscopy, including Fe_3Sn_2, Co_2MnGa, $PrAlGe$, Fe_3GeTe_2, $TbMn_6Sn_6$ and $Co_3Sn_2S_2$ [8, 13, 32–34]. Some of these materials exhibit high magnetic transition temperatures > 600 K, so that thermal broadening may fundamentally overwhelm magnetic evolution of the Weyl or Dirac state [8, 14]. Other systems, such as $PrAlGe$, exhibit low transition temperatures of ~ 10 K, associated with only small magnetic perturbations to the electronic structure [13]. Even in materials such as Fe_3GeTe_2, with intermediate $T_C = 230$ K, the thermal evolution appears to be dominated by a suppression of quasiparticle lifetime, without significant coherent evolution of the dispersion [35–37]. Using newly available high-quality single crystals combined with state-of-the-art variable-temperature photoemission spectroscopy, we have found that a large and previously overlooked energy shift of a topological spin-orbit gapped Weyl loop occurs in $Co_3Sn_2S_2$ across $T_C = 176$ K [38–43]. This shift takes place together with a magnetic exchange gap collapse that suggests a ferromagnetic Weyl to paramagnetic Dirac loop transition on raising temperature. This transition is further accompanied by the removal of candidate topological Fermi arc surface states and the annihilation of Weyl points.

Materials with inversion symmetry, mirror symmetry and ferromagnetism provide a unique platform for a magnetic-topological phase transition. The ferromagnetism produces singly-degenerate spin-split bands. In the limit of weak spin-orbit coupling (SOC), mirror

symmetry can then give rise to Weyl loops on mirror planes of the bulk Brillouin zone [8, 44–46]. A Weyl loop is a closed curve along which the bands are everywhere two-fold degenerate; it is characterized by a π Berry phase topological invariant and a linear energy-momentum dispersion everywhere along the loop. If the magnetic order is removed and no spin-splitting remains, opposite-spin partner Weyl loops naturally collapse into a Dirac loop, a closed curve along which the bands are everywhere four-fold degenerate [46–48]. Weyl loops under SOC typically gap out, concentrating a loop of Berry curvature in momentum space, leading to a giant anomalous Hall response [8, 10], large anomalous Nernst effect [29, 49], large optical Hall conductivity [40] and other exotic response. Under SOC, Weyl loops may also leave behind some discrete number of Weyl points. By contrast, Dirac points are generically unstable under inversion and time-reversal symmetry [50], so that Dirac loops under SOC gap out fully. As a result, in this scenario upon magnetic exchange collapse the Weyl points generically annihilate.

$Co_3Sn_2S_2$ crystallizes in space group $R\bar{3}2/m$ (No. 166), with dihedral point group D_{3d}, which includes inversion symmetry and three mirror planes (Fig. 1a, S3). The system is ferromagnetic, with Curie temperature $T_C = 176$ K [51, 52]. Keeping in mind the mirror symmetry and ferromagnetic order, we explore our $Co_3Sn_2S_2$ samples by ARPES at 20 K. Measuring with incident photon energy $h\nu = 130$ eV, we observe point-like electronic structures on M_y (cyan arrows, Fig. 1d; the mirror planes correspond to $\bar{\Gamma} - \bar{M}$). On cuts along k_y through the point-like features, we observe cone dispersions straddling the mirror plane M_y (Figs. 1e). On an energy-momentum cut along k_x, within the mirror plane, we again observe cone-like dispersions (Fig. S4). The observation of cone dispersions along both k_x and k_y, coming together at point Fermi surfaces, suggests a set of band crossings living in the momentum-space mirror plane. To systematically understand the evolution of the band crossings along the out-of-plane momentum-space direction k_z we acquire analogous datasets at a range of photon energies, from $h\nu = 100$ to 135 eV (Fig. S5). We find that the cones persist in $h\nu$, with crossing points consistently on the M_y plane, but at varying (k_x, k_z) coordinates (red diamonds, Fig. 1f). Taken together, these crossing points appear to form an extended nodal electronic state encircling the L point of the bulk Brillouin zone, suggesting the observation of a bulk loop node in $Co_3Sn_2S_2$. Since the system is ferromagnetic with generically singly-degenerate bands, we interpret this loop node as a Weyl loop (Fig. 1c). To extract the complete trajectory of the loop, we fit the ARPES

locations of the cone dispersions to a low-order polar Fourier decomposition around the L point of the bulk Brillouin zone (blue loop, Fig. 1f; see Supplemental Material [53] for fitting parameter values). In this way we extract the full momentum-space trajectory of the Weyl loop from photoemission data alone.

Next we explore the evolution of the Weyl loop with temperature, focusing on Cut (i). We systematically cycle the temperature of our samples from 20 K to 290 K and back to 20 K, moving across $T_C = 176$ K. On raising the temperature, we observe a dramatic evolution of the Weyl cone on a large energy scale of ~ 0.1 eV (Figs. 2a, b; S8), with the cone appearing to recede above E_F. We next assemble the momentum distribution curves (MDCs) of Cut (i) at E_F for all temperatures (Fig. 2c). Upon cycling the temperature, we observe a prominent and reversible evolution of the Weyl cone across T_C, consistent with a magnetic phase transition. For further insight, we examine additional spectra on Cut (ii), obtained during the course of the same measurement, and we consider a set of deep bands ~ 0.3 eV below E_F, which are predominantly formed from the same exchange-split Co $3d$ a_{1g} and e_g manifolds as the Weyl loop (Figs. 2d; S11). At 20 K, these deep valence bands exhibit clear splitting, consistent with the material's ferromagnetic order. Upon raising the temperature, the splitting appears to vanish and these deep bands collapse together, suggesting a paramagnetic state with spin-degenerate bands. By examining the evolution of the deep bands, we circumvent the limitations of the photoemission E_F cut-off and observe direct signatures of a prominent magnetic exchange gap collapse across T_C in $Co_3Sn_2S_2$.

To relate the Weyl loop temperature evolution to the magnetic exchange gap collapse, we consider more carefully the interplay between topology and ferromagnetism. In *ab initio* calculation, in the absence of SOC and in the ferromagnetic state, the Weyl loop arises as a crossing of two spin-majority bands, with a spin-minority partner Weyl loop above the Fermi level (schematic blue and green loops, Figs. 2e; S6). In a non-magnetic *ab initio* calculation, the exchange gap vanishes and these two Weyl loops coincide, forming a spinless loop crossing—a Dirac loop (purple loop). Comparing the *ab initio* calculations with ARPES, we find that the magnetic Weyl and non-magnetic Dirac nodes exhibit overall agreement with the ferromagnetic and paramagnetic spectra, respectively (magenta traces, Fig. 2b). Note that including SOC in our *ab initio* results does not alter this interpretation, although the expected gap appears in both loop nodes (blue traces). The observation that the loop recedes above E_F on increasing temperature is also consistent with maintenance of

charge balance in the spin-degenerate electronic structure, further indicating a paramagnetic Dirac loop. We further reduced the magnetic moment in our samples via nickel (Ni) doping, and again observed a persistent loop node electronic structure despite suppression of the ferromagnetism (Fig. S1). Taken together, our systematic ARPES spectra and *ab initio* calculations suggest that we have observed the collapse of two opposite-spin ferromagnetic Weyl loops into a paramagnetic Dirac loop.

To quantitatively characterize the Weyl loop collapse with temperature, we perform a Lorentzian fit of energy distribution curves (EDCs) through the extremum of the Weyl loop band (Cut(i), dotted line, Fig. 2a). The extracted Weyl band extremum exhibits a clear evolution upward in E_B as the temperature increases, 20 K $\rightarrow$ 250 K, consistent with exchange gap collapse (Fig. 2d). We further extract the exchange gap $\Delta(T)$ on EDCs through the deep bands (Cut (ii), dotted line, Fig. 2c) and compared the resulting $\Delta(T)$ with the magnetization $M(T)$ as measured by a SQUID. For $T < T_C$ we find that the exchange splitting tracks $M(T)$. For $T > T_C$ we no longer observe an exchange splitting within our spectral linewidth, consistent with the absence of magnetization. Remarkably, the observed exchange gap and Weyl band shift are both $\sim$ 0.12 eV, suggesting a complete collapse of the opposite-spin partner Weyl loops across T_C and the formation of a spin-degenerate paramagnetic Dirac loop.

To further explore the paramagnetic Dirac loop we park our apparatus at 220 K, well into the paramagnetic phase. At a range of $h\nu$ we observe characteristic point-like iso-energy contours on M_y and related mirror planes (Figs. 3a, c; S7). Energy-momentum spectra through these point-like contours further exhibit cone-like spectral weight straddling M_y, indicative of Dirac loop cone dispersions above E_F (Figs. 3b, d). The presence of multiple cone features straddling M_y at a range of $h\nu$ again suggests an extended nodal electronic structure confined to the mirror plane. Since we are in the paramagnetic phase with generically spin-degenerate bands, we interpret these candidate band crossings as four-fold degenerate, forming a Dirac loop. By analogy with our analysis in the ferromagnetic phase, we again systematically collect the locations of all cone features observed in the paramagnetic phase for $h\nu$ from 100 to 135 eV and experimentally extract the full momentum-space trajectory of the Dirac loop (red diamonds, Fig. 3e). *Ab initio* calculations of the Weyl and Dirac loops in the ferromagnetic and non-magnetic states also agree with the experimentally-observed trajectories (Fig. S2). A loop node electronic structure persisting into the paramagnetic

phase of $Co_3Sn_2S_2$ again suggests the observation of a ferromagnetic Weyl to paramagnetic Dirac loop collapse.

We next consider the fine structure of the Weyl loop collapse associated with spin-orbit coupling (SOC). In $Co_3Sn_2S_2$, *ab initio* calculations along with ARPES and STM investigations suggest that each Weyl loop under SOC produces two Weyl points above the Fermi level, with signatures of topological Fermi arc surface states extending below the Fermi level. [9–12, 38–41]. Our observation of a Weyl to Dirac loop transition naturally motivates investigation of Fermi arc and Weyl point annihilation across T_C. At 20 K, we observe sharp arc-shaped states near the expected Weyl points, consistent with topological Fermi arcs in *ab initio* calculation (Figs. 4a, c; S9). At 220 K these Fermi arcs vanish, leaving behind bulk pockets broadly consistent with the low temperature spectra (Figs. 4b, d). The disappearance of the Fermi arcs above T_C provides evidence for the annihilation of Weyl points in the paramagnetic phase. To further characterize this annihilation, we consider the *ab initio* band structure under ferromagnetic order on a momentum-space path connecting a pair of exchange-split Weyl points (Fig. 4e). Upon exchange collapse, these partner Weyl points come together and annihilate, opening a gap (Fig. 4f).

Our systematic variable-temperature ARPES experiments suggest that pairs of ferromagnetic Weyl loops collapse into paramagnetic Dirac loops across T_C in $Co_3Sn_2S_2$ (Figs. 4g, h). Taken together with *ab initio* calculations, our results additionally provide evidence for the annihilation of Fermi arcs and Weyl points concomitant with this transition. Our findings suggest a general mechanism for Weyl fermion annihilation, where the annihilation is driven by magnetic exchange gap collapse and takes place predominantly along the energy axis, rather than in momentum [3, 21, 54]. This novel mechanism should occur naturally in many quantum magnets and motivates exploration of the rich topological evolution associated with the onset of magnetic order. Such interplay between magnetism and topology may also pave the way to magnetic design of correlated topological states with exotic transport and optical response.

ACKNOWLEDGMENTS

---

† Electronic address: ilya.belopolski@riken.jp

‡ Electronic address: mzhasan@princeton.edu

[1] E. H. da Silva Neto, "Weyl"ing away time-reversal symmetry. *Science* **365**, 1248 (2019).

[2] N. P. Armitage, E. J. Mele, A. Vishwanath, Weyl and Dirac semimetals in three-dimensional solids. *Rev. Mod. Phys.* **90**, 015001 (2018).

[3] M. Z. Hasan, S.-Y. Xu, I. Belopolski, S.-M. Huang, Discovery of Weyl fermion semimetals and topological Fermi arc states. *Ann. Rev. Cond. Matt. Phys.* **8**, 289 (2017).

[4] J. Maciejko, G. A. Fiete, Fractionalized topological insulators. *Nat. Phys.* **11**, 385 (2015).

[5] M. Z. Hasan, *et al.*, Weyl, Dirac and high-fold chiral fermions in topological quantum matter. *Nat. Rev. Mat.* (2021).

[6] B. Keimer, J. E. Moore, The physics of quantum materials. *Nat. Phys.* **13**, 1045 (2017).

[7] D. N. Basov, R. D. Averitt, D. Hsieh, Towards properties on demand in quantum materials. *Nat. Mat.* **16**, 1077 (2017).

[8] I. Belopolski, *et al.*, Discovery of topological Weyl fermion lines and drumhead surface states in a room temperature magnet. *Science* **365**, 1278 (2019).

[9] Q. Wang, *et al.*, Large intrinsic anomalous Hall effect in half-metallic ferromagnet $Co_3Sn_2S_2$ with magnetic Weyl fermions. *Nat. Commun.* **9**, 3681 (2018).

[10] E. Liu, *et al.*, Giant anomalous Hall effect in a ferromagnetic kagome-lattice semimetal. *Nat. Phys.* **14**, 1125 (2018).

[11] N. Morali, *et al.*, Fermi-arc diversity on surface terminations of the magnetic Weyl semimetal $Co_3Sn_2S_2$. *Science* **365**, 1286 (2019).

[12] D. F. Liu, *et al.*, Magnetic Weyl semimetal phase in a Kagomé crystal. *Science* **365**, 1282 (2019).

[13] D. S. Sanchez, *et al.*, Observation of Weyl fermions in a magnetic non-centrosymmetric crystal. *Nat. Commun.* **11**, 3356 (2020).

[14] L. Ye, *et al.*, Massive Dirac fermions in a ferromagnetic kagome metal. *Nature* **555**, 638 (2018).

[15] J. Hu, S.-Y. Xu, N. Ni, Z. Mao, Transport of topological semimetals. *Ann. Rev. Cond. Mat. Phys.* **49**, 207 (2019).

[16] J. Xiong, *et al.*, Evidence for the chiral anomaly in the Dirac semimetal Na_3Bi. *Science* **350**, 413 (2015).

[17] C.-L. Zhang, *et al.*, Magnetic-tunnelling-induced Weyl node annihilation in TaP. *Nat. Phys.* **13**, 979 (2017).

[18] K. Manna, *et al.*, From Colossal to Zero: Controlling the Anomalous Hall Effect in Magnetic

Heusler Compounds via Berry Curvature Design. *Phys. Rev. X* **8**, 041045 (2018).

[19] A. Sakai, *et al.*, Giant anomalous Nernst effect and quantum-critical scaling in a ferromagnetic semimetal. *Nat. Phys.* **14**, 1119 (2018).

[20] K. Kuroda, *et al.*, Evidence for magnetic Weyl fermions in a correlated metal. *Nat. Mat.* **16**, 1090 (2017).

[21] A. A. Burkov, L. Balents, Weyl Semimetal in a Topological Insulator Multilayer. *Phys. Rev. Lett.* **107**, 127205 (2011).

[22] X. Wan, A. M. Turner, A. Vishwanath, S. Y. Savrasov, Topological semimetal and Fermi-arc surface states in the electronic structure of pyrochlore iridates. *Phys. Rev. B* **83**, 205101 (2011).

[23] A. A. Zyuzin, S. Wu, A. A. Burkov, Weyl semimetal with broken time reversal and inversion symmetries. *Phys. Rev. B* **85**, 165110 (2012).

[24] S. F. Islam, A. A. Zyuzin, Collective modes in imbalanced nodal line semimetal (2021). arXiv:2108.13951.

[25] S. Zhong, J. E. Moore, I. Souza, Gyrotropic magnetic effect and the magnetic moment on the fermi surface. *Phys. Rev. Lett.* **116**, 077201 (2016).

[26] Q. Ma, *et al.*, Direct optical detection of Weyl fermion chirality in a topological semimetal. *Nat. Phys.* **13**, 842 (2017).

[27] G. B. Osterhoudt, *et al.*, Colossal mid-infrared bulk photovoltaic effect in a type-i weyl semimetal. *Nat. Mat.* **18**, 471 (2019).

[28] S. S.-L. Zhang, A. A. Burkov, I. Martin, O. G. Heinonen, Spin-to-Charge Conversion in Magnetic Weyl Semimetals. *Phys. Rev. Lett.* **123**, 187201 (2019).

[29] A. Sakai, *et al.*, Iron-based binary ferromagnets for transverse thermoelectric conversion. *Nature* **581**, 53 (2020).

[30] J. C. W. Song, M. S. Rudner, Fermi arc plasmons in Weyl semimetals. *Phys. Rev. B* **96**, 205443 (2017).

[31] F. Adinehvand, Z. Faraei, T. Farajollahpour, S. A. Jafari, Sound of Fermi arcs: a linearly dispersing gapless surface plasmon mode in undoped Weyl semimetals. *Phys. Rev. B* **100**, 195408 (2019).

[32] J.-X. Yin, *et al.*, Giant and anisotropic many-body spin-orbit tunability in a strongly correlated kagome magnet. *Nature* (2018).

[33] J.-X. Yin, *et al.*, Quantum-limit Chern topological magnetism in $TbMn_6Sn_6$. *Nature* **583**, 533 (2020).

[34] J.-X. Yin, *et al.*, Negative flat band magnetism in a spin-orbit-coupled correlated kagome magnet. *Nat. Phys.* **15**, 443 (2019).

[35] K. Kim, *et al.*, Large anomalous Hall current induced by topological nodal lines in a ferromagnetic van der Waals semimetal. *Nat. Mat.* **17**, 794 (2018).

[36] Y. Zhang, *et al.*, Emergence of Kondo lattice behavior in a van der Waals itinerant ferromagnet, Fe_3GeTe_2. *Sci. Adv.* **4**, eaao6791 (2018).

[37] X. Xu, *et al.*, Signature for non-Stoner ferromagnetism in the van der Waals ferromagnet Fe_3GeTe_2. *Phys. Rev. B* **101**, 201104 (2020).

[38] Q. Xu, *et al.*, Topological surface Fermi arcs in the magnetic Weyl semimetal $Co_3Sn_2S_2$. *Phys. Rev. B* **97**, 235416 (2018).

[39] Z. Guguchia, *et al.*, Tunable anomalous Hall conductivity through volume-wise magnetic competition in a topological kagome magnet. *Nat. Commun.* **11**, 559 (2020).

[40] Y. Okamura, *et al.*, Giant magneto-optical responses in magnetic Weyl semimetal $Co_3Sn_2S_2$. *Nat. Commun.* **11**, 4619 (2020).

[41] R. Yang, *et al.*, Magnetization-Induced Band Shift in Ferromagnetic Weyl Semimetal $Co_3Sn_2S_2$. *Phys. Rev. Lett.* **124**, 077403 (2020).

[42] A. Rossi, *et al.*, Electronic structure and topology across T_C in magnetic Weyl semimetal $Co_3Sn_2S_2$ (2021). arXiv:2105.08265.

[43] D. F. Liu, *et al.*, Topological Phase Transition in a Magnetic Weyl Semimetal (2021). arXiv:2106.03229.

[44] Y. Wang, R. Nandkishore, Topological surface superconductivity in doped Weyl loop materials. *Phys. Rev. B* **95**, 060506 (2017).

[45] O. Stenull, C. L. Kane, T. C. Lubensky, Topological phonons and Weyl lines in three dimensions. *Phys. Rev. Lett.* **117**, 068001 (2016).

[46] R. Nandkishore, Weyl and Dirac loop superconductors. *Phys. Rev. B* **93**, 020506(R) (2016).

[47] Y. Kim, B. J. Wieder, C. L. Kane, A. M. Rappe, Dirac line nodes in inversion-symmetric crystals. *Phys. Rev. Lett.* **115**, 036806 (2015).

[48] A. Yamakage, Y. Yamakawa, Y. Tanaka, Y. Okamoto, Line-Node Dirac Semimetal and Topological Insulating Phase in Noncentrosymmetric Pnictides $CaAgX$ (X = P, As). *J. of the*

Phys. Soc. of Jpn. **85**, 013708 (2016).

[49] S. N. Guin, *et al.*, Zero-Field Nernst Effect in a Ferromagnetic Kagome-Lattice Weyl-Semimetal $Co_3Sn_2S_2$. *Adv. Mat.* **31**, 1806622 (2019).

[50] S. Murakami, Phase transition between the quantum spin Hall and insulator phases in 3D: emergence of a topological gapless phase. *New J. Phys.* **9**, 356 (2007).

[51] P. Vaqueiro, G. G. Sobany, A powder neutron diffraction study of the metallic ferromagnet $Co_3Sn_2S_2$. *Solid State Sci.* **11**, 513 (2009).

[52] W. Schnelle, *et al.*, Ferromagnetic ordering and half-metallic state of $Sn_2Co_3S_2$ with the shandite-type structure. *Phys. Rev. B* **88**, 144404 (2013).

[53] See Supplemental Material at [url] for methods and additional systematics, including Refs. [55–62].

[54] S.-M. Huang, *et al.*, A Weyl Fermion semimetal with surface Fermi arcs in the transition metal monopnictide TaAs class. *Nat. Commun.* **6**, 7373 (2015).

[55] G. S. Thakur, *et al.*, Intrinsic Anomalous Hall Effect in Ni-Substituted Magnetic Weyl Semimetal $Co_3Sn_2S_2$. *Chem. Mat.* **32**, 1612 (2020).

[56] M. Hoesch, *et al.*, A facility for the analysis of the electronic structures of solids and their surfaces by synchrotron radiation photoelectron spectroscopy. *Rev. Sci. Inst.* **88**, 013106 (2017).

[57] G. Kresse, J. Furthmueller, Efficient iterative schemes for *ab initio* total-energy calculations using a plane-wave basis set. *Phys. Rev. B* **54**, 11169 (1996).

[58] G. Kresse, J. Furthmueller, Efficiency of ab-initio total energy calculations for metals and semiconductors using a plane-wave basis set. *Comp. Mat. Sci.* **6**, 15 (1996).

[59] J. P. Perdew, K. Burke, M. Ernzerhof, Generalized gradient approximation made simple. *Phys. Rev. Lett.* **77**, 3865 (1996).

[60] Q. S. Wu, S. Zhang, H.-F. Song, M. Troyer, A. A. Soluyanov, WannierTools: an open-source software package for novel topological materials. *Comput. Phys. Commun.* **224**, 405 (2018).

[61] G. Pizzi, *et al.*, Wannier90 as a community code: new features and applications. *J. Phys.: Cond. Mat.* **32**, 165902 (2020).

[62] G. Li, *et al.*, Surface states in bulk single crystal of topological semimetal $Co_3Sn_2S_2$ toward water oxidation. *Sci. Adv.* **5**, eaaw9867 (2019).
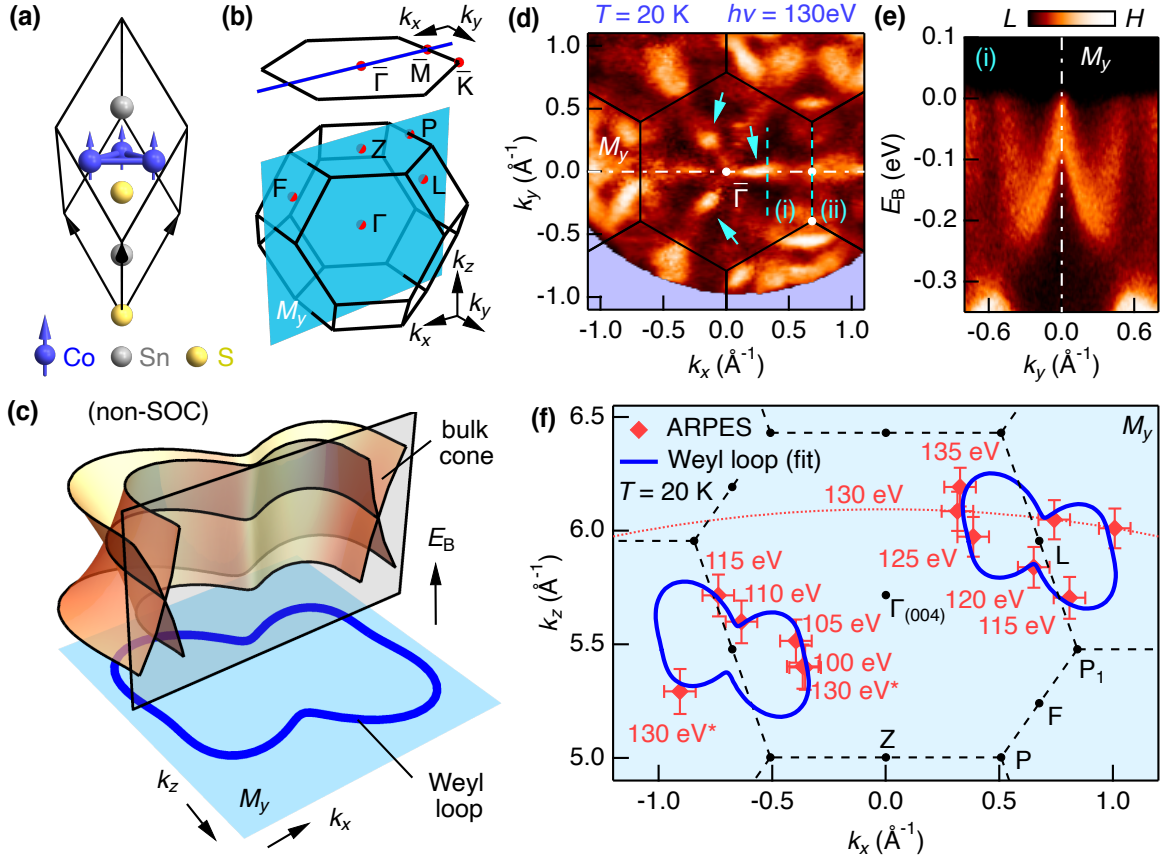
FIG. 1: **Topological magnetic Weyl loop.** (a) Primitive unit cell of ferromagnetic $Co_3Sn_2S_2$, with mirror symmetry. (b) Bulk and (001) surface Brillouin zones with bulk mirror plane (M_y, cyan) and several high-symmetry points (red). (c) In the absence of spin-orbit coupling (SOC), the combination of mirror symmetry and ferromagnetism generically gives rise to Weyl loops, which live in the mirror planes of the bulk Brillouin zone. A Weyl loop exhibits a ring of band crossings along a closed curve in momentum space (blue loop) with a linear cone dispersion on any energy-momentum slice through the loop. Under SOC, the Weyl loop typically gaps, possibly leaving behind Weyl points. (d) ARPES Fermi surface at $T = 20$ K and photon energy $h\nu = 130$ eV, exhibiting multiple dot features (cyan arrows) on the mirror planes ($\bar{\Gamma} - \bar{M}$). (e) Cone dispersion at the Fermi level on an energy-momentum spectrum through the dot feature (Cut i). (f) Collecting cone dispersions for a range of $h\nu$ suggests a loop of band crossings (red diamonds) living in M_y and encircling the bulk L point (Fig. S4, S5). Different $h\nu$ sample different out-of-plane k_z momenta; representative example shown for 130 eV (dotted red curve). The crossing points can be fit by a low-order polar coordinate Fourier decomposition around the L point (blue curve [53]), mapping out the trajectory of the Weyl loop.
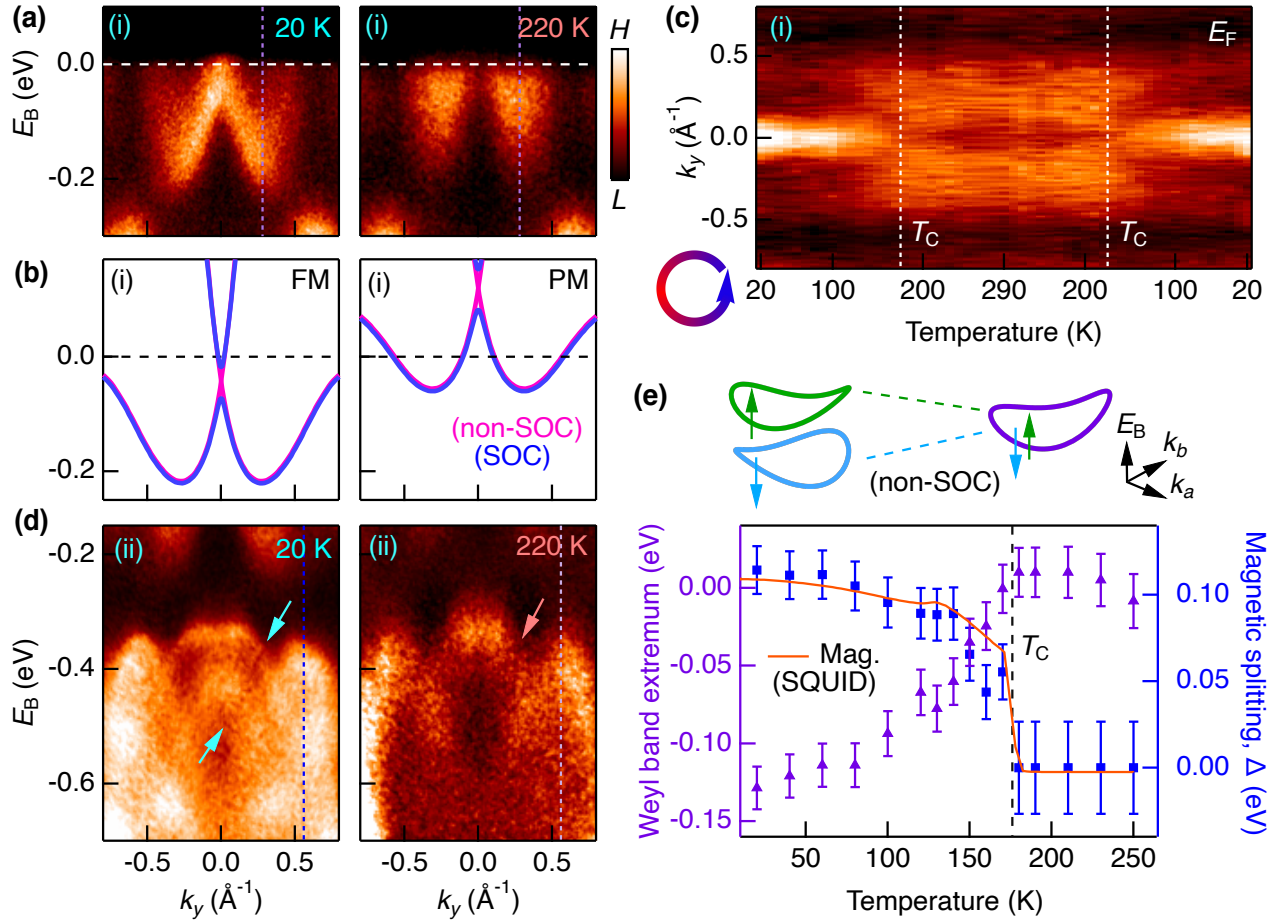
14

FIG. 2: **Magnetic Weyl to Dirac loop collapse.** (**a**) Cut (i) at 20 K and 220 K, with (**b**) corresponding *ab initio* calculation. Left: calculation in the ferromagnetic state through the Weyl loop, without SOC (magenta) and with SOC (blue). Right: calculation in the non-magnetic state through the Dirac loop. (**c**) Momentum distribution curves (MDCs) of Cut (i) at the Fermi level for the full temperature cycle, 20 K → 290 K → 20 K. (**d**) Cut (ii), defined in Fig. 1d, exhibiting clear splittings in deeper energy bands at 20 K (left), which collapse at 220 K (right). (**e**) Energy extremum of the Weyl loop band, extracted from the temperature dependence on Cut (i), obtained by Lorentzian fitting of energy distribution curves (EDCs, dotted lines in (a)). Also, the magnetic exchange splitting as a function of temperature, obtained from Cut (ii) by Lorentzian fitting to EDCs (dotted lines in (d)) and compared with the magnetization $M(T)$. Cartoon: exchange gap collapse of two opposite-spin Weyl loop partners (blue and green) into a single Dirac loop (purple).
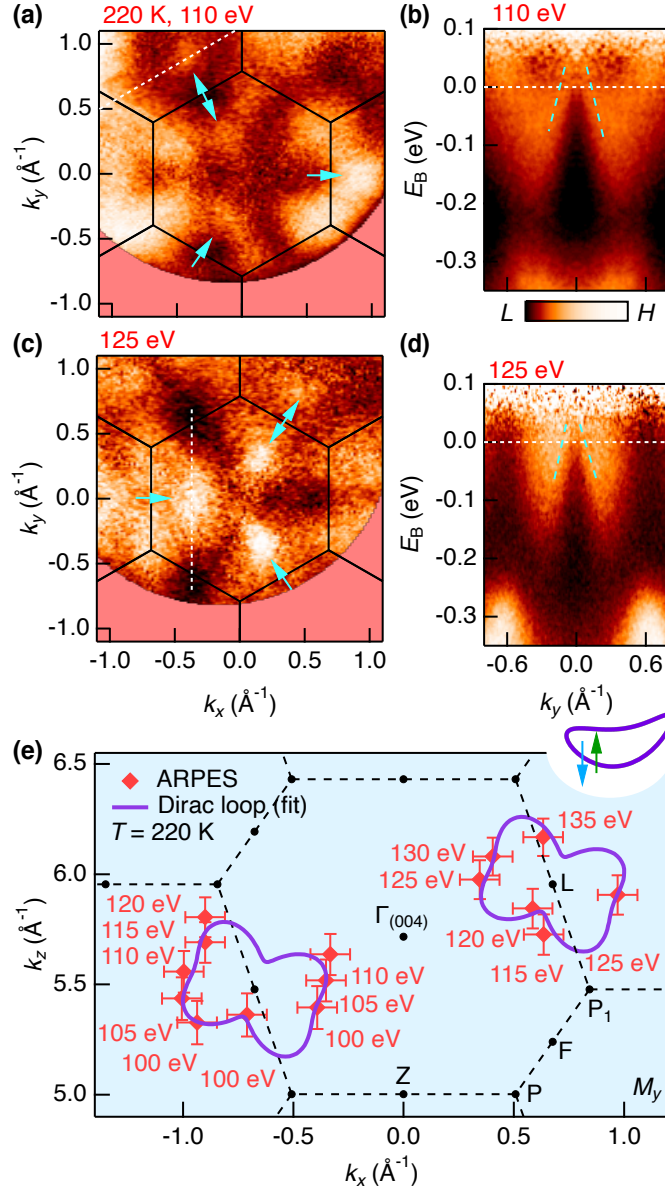
FIG. 3: **Paramagnetic Dirac loop.** (**a**) ARPES iso-energy contour slightly above E_F, at $h\nu =$ 110 eV, acquired at 220 K, exhibiting point-like features (cyan arrows) along $\bar{\Gamma} - \bar{M}$ (corresponding to M_y and the symmetry-related mirror planes). (**b**) Energy-momentum cut through the point-like feature, exhibiting cone-like spectral weight (cut location: white line in (a)). (**c**), (**d**) Analogous to (a), (b), at 125 eV. (**e**) Locations of cones observed for all $h\nu$ (red diamonds, Fig. S7). Cones on symmetry-related mirror planes are plotted all together in a single momentum-space mirror plane M_y. Data points fit to a low-order polar coordinate Fourier decomposition around L (purple curves), mapping out the trajectory of the Dirac loop.
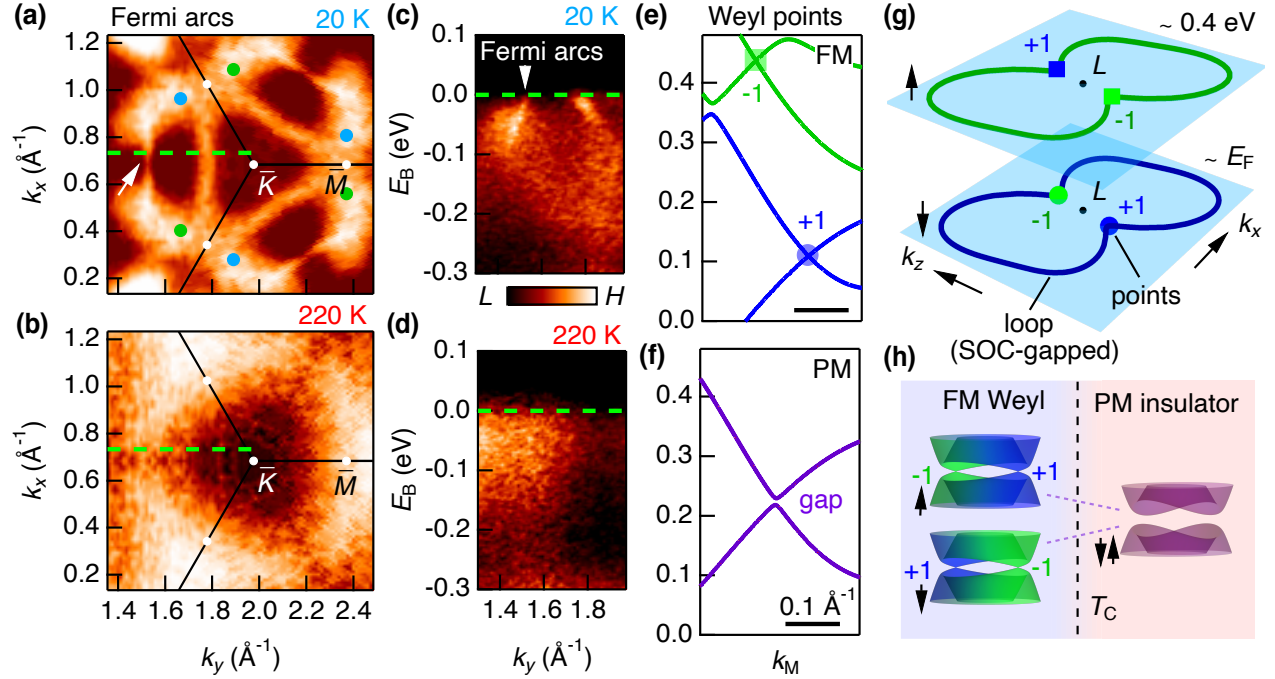
FIG. 4: **Evidence for Fermi arc and Weyl point annihilation.** (**a**) Fermi surface acquired at $T = 20$ K, $h\nu = 130$ eV, exhibiting candidate Fermi arc surface states (white arrow) near the Weyl point locations, as predicted by *ab initio* calculations (blue, green circle; Fig. S9). Data symmetrized for clarity. (**b**) Analogous Fermi surface at 220 K, with no signature of Fermi arcs. (**c**) Energy-momentum cut through the candidate Fermi arcs at 20 K (green dotted line, (a)). (**d**) Analogous cut at 220 K. (**e**) Calculation in the ferromagnetic state, in the presence of SOC, slicing through a pair of exchange-split Weyl points of opposite chirality. (**f**) Analogous calculation, non-magnetic state. The two partner Weyl points annihilate, opening a gap of 12 meV. (**g**) Schematic of the ferromagnetic Weyl loop (non-SOC) and Weyl point (SOC) configuration. (**h**) Schematic phase diagram: spin-orbit gapped ferromagnetic Weyl loops collapse to a paramagnetic Dirac loop across $T_{\rm C}$. Concurrently, the exchange-split Weyl points annihilate.

Supplemental Material for:

Signatures of Weyl fermion annihilation

in a correlated kagome magnet

Ilya Belopolski*, Tyler A. Cochran*, Xiaoxiong Liu*, Zi-Jia Cheng*, Xian P. Yang, Zurab Guguchia, Stepan S. Tsirkin, Jia-Xin Yin, Praveen Vir, Gohil S. Thakur, Songtian S. Zhang, Junyi Zhang, Konstantine Kaznatcheev, Guangming Cheng, Guoqing Chang, Daniel Multer, Nana Shumiya, Maksim Litskevich, Elio Vescovo, Timur K. Kim, Cephise Cacho, Nan Yao, Claudia Felser, Titus Neupert, and M. Zahid Hasan

WEYL LOOP IN MAGNETICALLY-SUPPRESSED Ni-DOPED Co$_3$Sn$_2$S$_2$

We can more deeply explore the ferromagnetic Weyl to paramagnetic Dirac loop transition in nickel (Ni) doped Co$_3$Sn$_2$S$_2$. Our Ni$_x$Co$_{3-x}$Sn$_2$S$_2$ samples show a well-behaved suppression of ferromagnetism upon increased dopant concentration, with approximately linear decay to zero of the T_C, the magnetization M and the anomalous Hall conductivity σ_{xy}^A as the Ni level varies from $x = 0$ to 0.6 [55]. At the same time, Ni nominally electron dopes the system. This allows photoemission measurements in a reduced-magnetization state with favorable positioning of the Fermi level, while maintaining base temperature for the measurement and consequently providing higher energy resolution. At $x = 0.35$, for $h\nu = 110$ eV, we observe clear point-like Fermi surfaces with sharp cone dispersion (Figs. S1a,b). This cone dispersion persists for a range of $h\nu$, suggesting that the loop node electronic structure survives in the reduced-magnetization state, again indicating a magnetic Weyl to Dirac loop transition as ferromagnetism is suppressed (Fig. S1c-f). The momentum-space trajectory of the Ni-doped loop node (green diamonds, Fig. S2) quantitatively agrees with the Weyl and Dirac loop trajectories extracted for the undoped sample. These systematic results further support a ferromagnetic Weyl to paramagnetic Dirac loop transition.

METHODS

Single crystal growth: Single crystals of Co$_3$Sn$_2$S$_2$ were grown by a self-flux method with the congruent composition. The stoichiometrically-weighted starting materials were put in a graphite crucible sealed in a quartz tube. The samples were heated to 1000°C over 48 hours, left there for 24 hours, and then slowly cooled to 600°C over one week. An annealing process was implemented at 600°C for another 24 hours to produce homogeneous and well-ordered crystals. The compositions and phase structure of the samples were initially checked by energy-dispersive X-ray spectroscopy and powder X-ray diffraction, respectively.

Scanning transmission electron microscopy: Thin lamellae for microstructure characterization were prepared from bulk single crystals by focused ion beam cutting using a FEI Helios NanoLab 600 dual beam system (FIB/SEM). Atomic resolution high-angle annular dark-field (HAADF) scanning transmission electron microscopy (STEM) imaging

and atomic-level energy-dispersive X-ray spectroscopy (EDS) mapping were performed on a double Cs-corrected FEI Titan Cubed Themis 300 scanning/transmission electron microscope (S/TEM) equipped with an X-FEG source operated at 300 kV with a Super-X EDS system.

Magnetometry: The magnetization measurement was carried out with a superconducting quantum interference device (SQUID) magnetometer (QuantumDesign) from 2 to 300 K in a magnetic field of 0.01 T applied parallel to the crystallographic c-axis.

Angle-resolved photoemission spectroscopy: Photon-energy-dependent ARPES measurements were carried out at Beamline I05 of Diamond Light Source, Harwell Science Campus, Oxfordshire, UK using a Scienta R4000 electron analyzer with angular resolution $< 0.2°$ and total energy resolution < 13 meV for all photon energies, from 100 to 135 eV, with spot size 50 μm $\times$ 50 μm [56]. The sample temperature was 8 K. Temperature-dependent ARPES measurements were carried out at Beamline 5-2 of the Stanford Synchrotron Radiation Lightsource, SLAC in Menlo Park, CA, USA using a Scienta R4000 electron analyzer, with photon energy $h\nu = 130$ eV; angular resolution $< 0.2°$; total energy resolution from 14 meV at 22 K to 30 meV at 280 K; and beam spot size 16 μm (vertical) $\times$ 36 μm (horizontal). Measurements on $Ni_xCo_{3-x}Sn_2S_2$ samples were carried out at Beamline 21-ID-1 (ESM-ARPES) of the National Synchrotron Light Source II, BNL in Upton, NY, USA. Samples were cleaved *in situ* and measured under a vacuum of 4×10^{-11} Torr or better for all temperatures. To characterize the Weyl and Dirac loops, it is natural to parametrize its trajectory by an angle ω in polar coordinates with L taken as the origin. The loop is then described by a function $r(\omega)$ with 2π periodicity. Crystalline inversion symmetry P further requires that the dispersion remain unchanged under inversion through L, constraining the trajectory to $r(\omega + \pi) = r(\omega)$. With π periodicity, the first three terms of the Fourier decomposition are $r(\omega) = r_0 + r_1 \cos(2\omega + \phi_1) + r_2 \cos(4\omega + \phi_2)$. By fitting to the ARPES locations of the cone dispersions, we find that the trajectory of the Weyl loop is given by $r_0 = 0.27$ Å^{-1}, $r_1 = 0.12$ Å^{-1}, $\phi_1 = 43°$, $r_2 = -0.05$ Å^{-1} and $\phi_2 = 27°$ (blue loop, Fig. 1f). In this way, we extract the full momentum-space trajectory of the Weyl and Dirac loops from photoemission data alone.

To understand the role of different surface terminations in our ARPES measurements, we cleaved 53 $Co_3Sn_2S_2$ crystals and imaged the cleaved surface by scanning tunneling microscopy (STM). We scanned ~ 10 μm^2 for every cleaved sample surface. We found that 33% of the surfaces are disordered (without atomic lattice), 50% are Sn surfaces, 15% are S surfaces and 2% are Co_3Sn surfaces. Moreover, our high-quality photoemission spectra of the surface states were consistently well-captured by *ab initio* calculations with Sn termination, but not S termination (Figs. S9, S10) [12]. Our systematic STM, ARPES and *ab initio* characterization suggests that only the Sn termination is relevant for our analysis.

Ab initio calculations: Density functional theory (DFT) calculations with the projected augmented wave (PAW) method were implemented in the Vienna *ab initio* simulation package (VASP) [57, 58] with generalized gradient approximation (GGA) [59]. For the irreducible Brillouin zone, k-meshes of size $8 \times 8 \times 8$ were used. The Fermi level of the *ab initio* calculation was also optimized to match the experimental results. The surface spectral function calculated by the WannierTools package [60], using a tight-binding model generated from maximally-localized Wannier functions [61]. It was observed that the Sn termination captured the essential features of the ARPES.
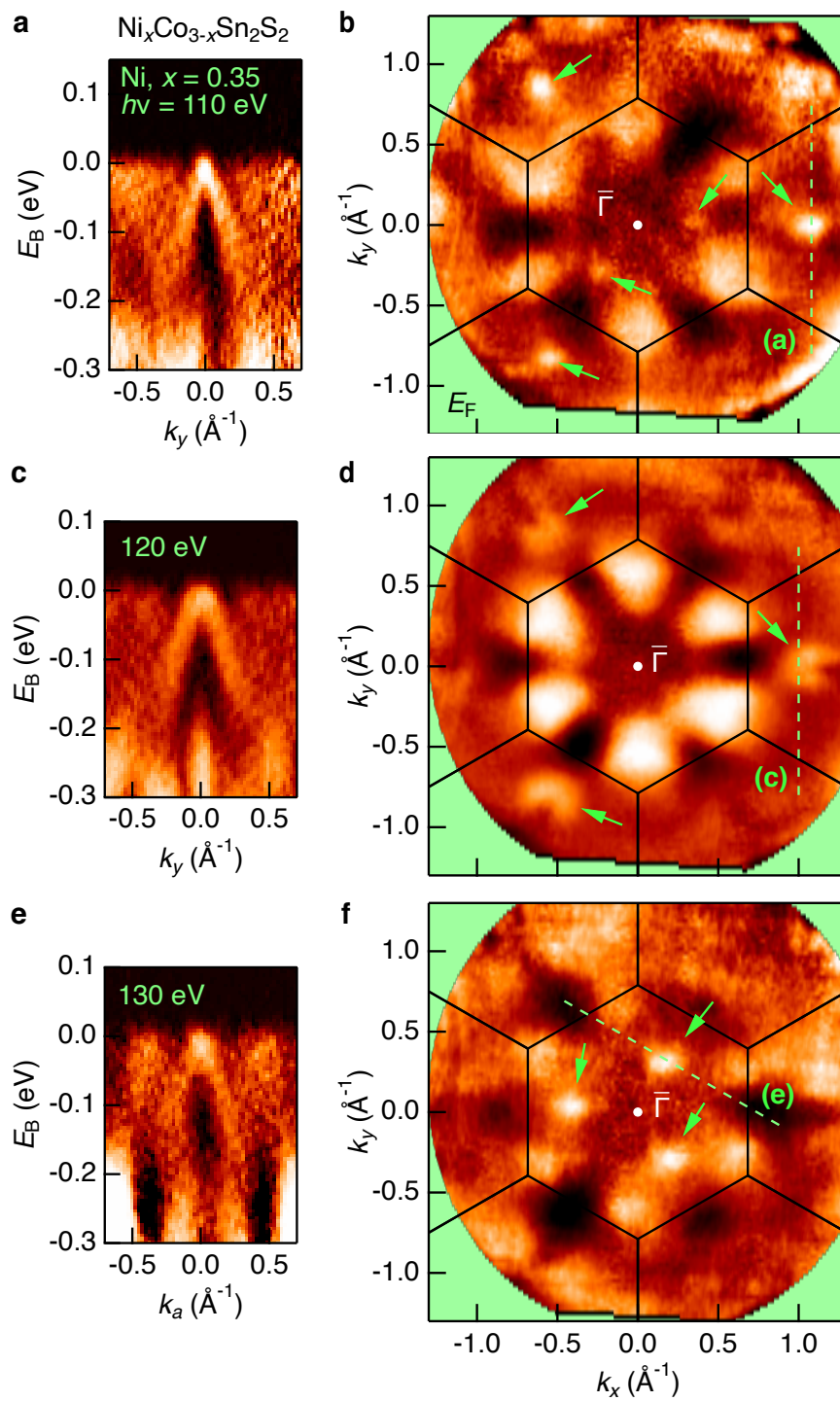
a

Ni$_x$Co$_{3-x}$Sn$_2$S$_2$

Ni, x = 0.35
$h\nu$ = 110 eV

E_B (eV)

k_y (Å^{-1})

b

k_y (Å^{-1})

$\bar{\Gamma}$

(a)

E_F

c

120 eV

E_B (eV)

k_y (Å^{-1})

d

k_y (Å^{-1})

$\bar{\Gamma}$

(c)

e

130 eV

E_B (eV)

k_a (Å^{-1})

f

k_y (Å^{-1})

$\bar{\Gamma}$

(e)

k_x (Å^{-1})

FIG. S1: **Weyl loop, Ni-doped Co$_3$Sn$_2$S$_2$.** (**a**) Energy-momentum ARPES spectrum obtained on ferromagnetically-suppressed Ni$_x$Co$_{3-x}$Sn$_2$S$_2$ single crystals, $x = 0.35$, at $T = 20$ K and $h\nu = 110$ eV, exhibiting a cone dispersion centered on M_y. (**b**) Corresponding Fermi surface at 110 eV, exhibiting point-like features (green arrows) on M_y and symmetry-equivalent mirror planes. Spectrum in (d) marked by the dotted green line. (**c**)-(**f**) Analogous spectra acquired at $h\nu = 120$ and 130 eV. The energy-momentum spectra again show clear cone dispersions (c, e), corresponding to point-like features (green arrows, d, f) on M_y and equivalent mirror planes.
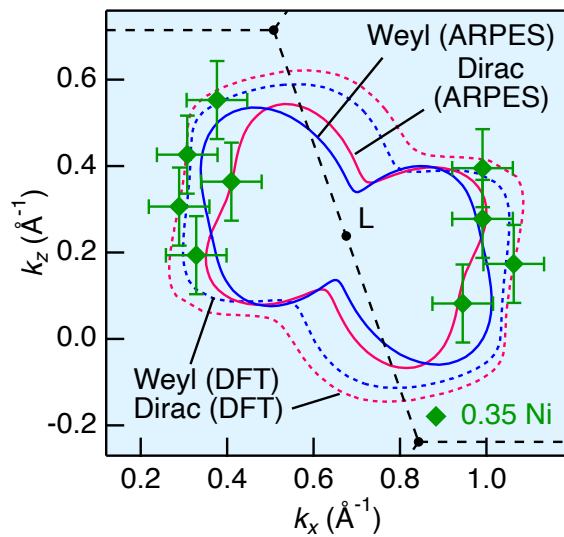
FIG. S2: **Loop node trajectories.** Summary of the ferromagnetic Weyl and paramagnetic Dirac loop trajectories extracted by photoemission; the analogous *ab initio* result in the ferromagnetic and non-magnetic states, in the absence of SOC; and cone dispersions observed in $Ni_xCo_{3-x}Sn_2S_2$.
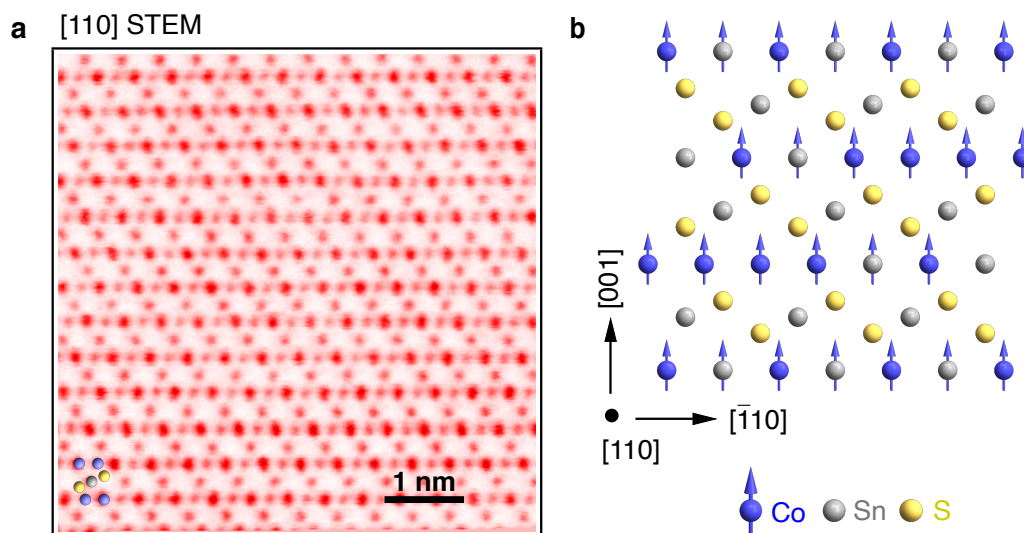
FIG. S3: **Crystal structure.** (a) Crystal structure of $Co_3Sn_2S_2$ along [110], measured by scanning transmission electron microscopy (STEM). (b) Schematic crystal structure viewed along [110], exhibiting the two-fold rotation C_{2x} symmetry.
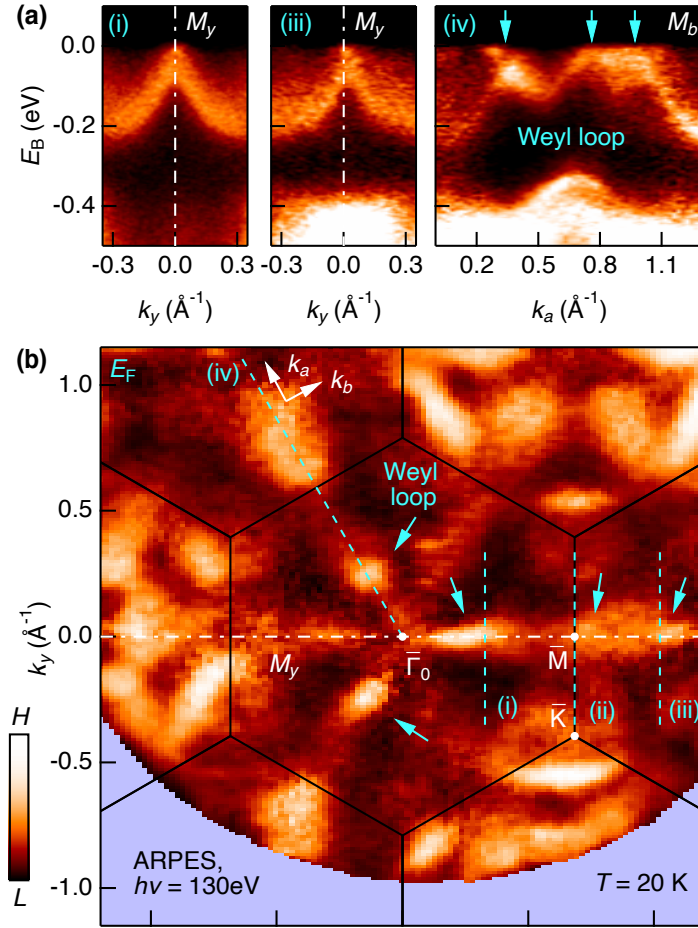
FIG. S4: **Systematics, Weyl loop.** (**a**) Multiple cone-like dispersions near the Fermi level in energy-momentum ARPES spectra of $Co_3Sn_2S_2$, acquired at $T = 20$ K and photon energy $h\nu = 130$ eV. Cut (i), (iii): transverse to the mirror plane. Cut (iv): contained within the mirror plane. Cut (iv) leftmost arrow: signatures of a hybridization gap with energy scale ~ 10 meV, consistent with the moderate SOC in $Co_3Sn_2S_2$ and suggestive of an SOC-gapped Weyl loop. Cut (ii): see main text. (**b**) ARPES Fermi surface exhibiting multiple dot features (cyan arrows) on the mirror planes (corresponding to $\bar{\Gamma} - \bar{M}$). The dots match up with the cone dispersions in (a).
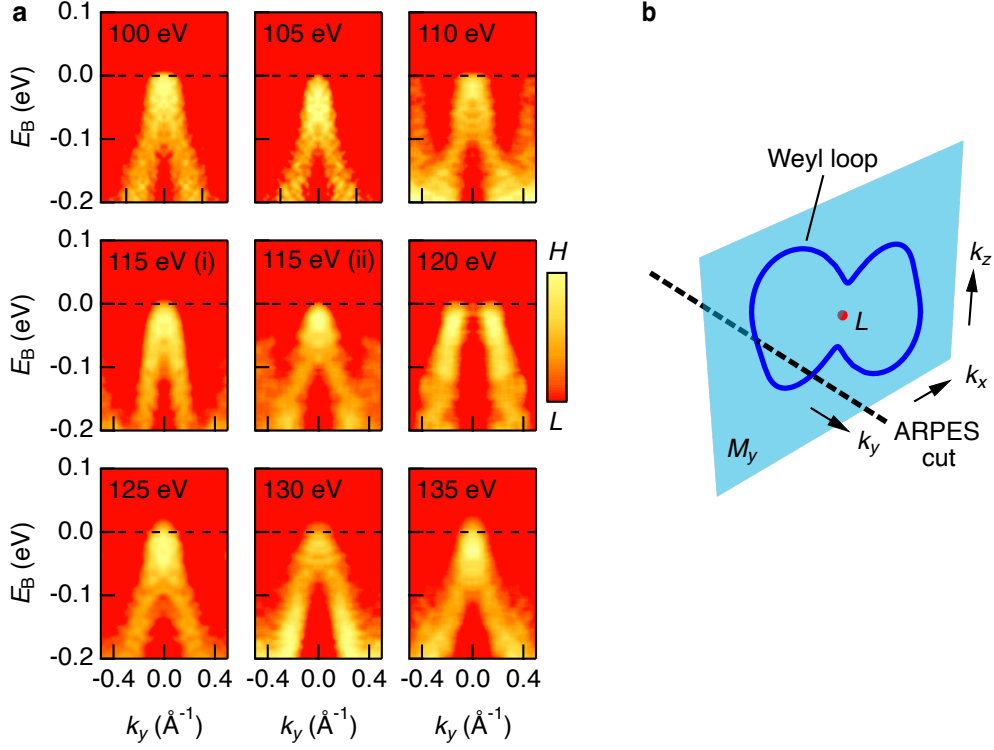
FIG. S5: **Systematics, Weyl loop.** (**a**) Additional source ARPES energy-momentum spectra used to extract the Weyl loop trajectory in Fig. 1f. At each value of $h\nu$ from 100 eV to 135 eV, we examined energy-momentum cuts upon sweeping in k_x, collecting all spectra exhibiting cone dispersions. (**b**) Converting $h\nu$ to k_z, we then assembled the resulting (k_x, k_z) coordinates to obtain the Weyl loop trajectory. Spectra symmetrized around $k_y = 0$ Å^{-1}.
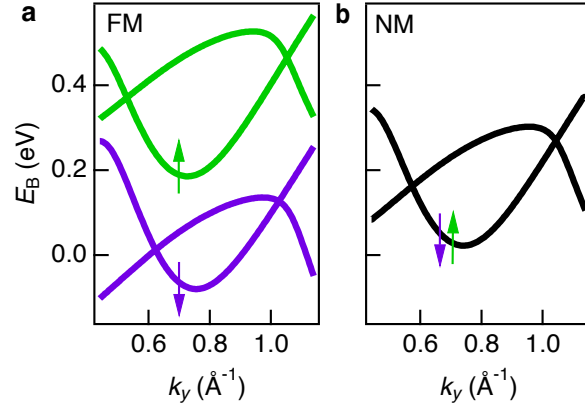
FIG. S6: **Weyl to Dirac loop collapse.** (a) *Ab initio* calculation in the ferromagnetic state, in the absence of SOC. The Weyl loop near E_F is formed from two majority spin bands with a partner Weyl loop of the opposite spin ~ 0.4 eV above E_F. (b) *Ab initio* calculation in the non-magnetic state, in the absence of SOC. The two opposite-spin Weyl loops collapse into a single Dirac loop, characterized by a spinless band crossing along a loop.
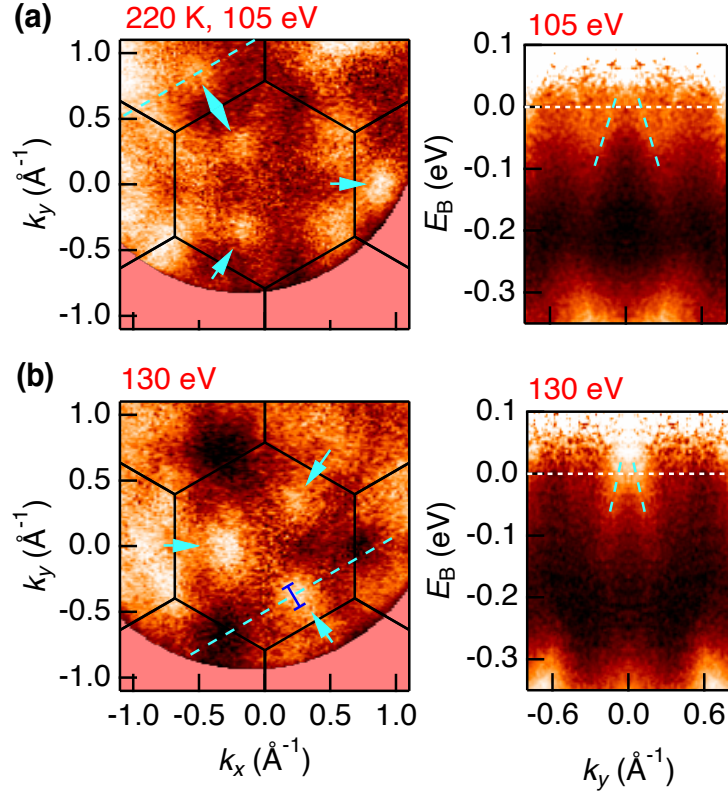
FIG. S7: **Systematics, Dirac loop.** (a), (b) Additional source ARPES energy-momentum spectra used to extract the Dirac loop trajectory in Fig. 3e, acquired at $h\nu$ as indicated.
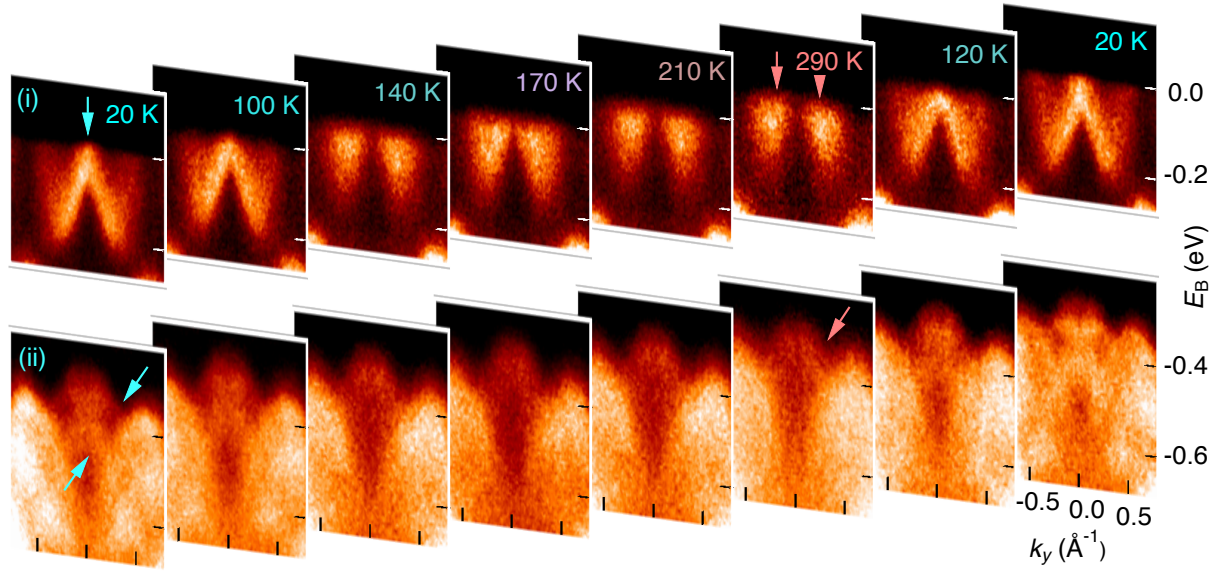
FIG. S8: **Systematics, temperature dependence.** Evolution of the Weyl loop and deep valence bands under temperature cycling, 20 K → 290 K → 20 K.
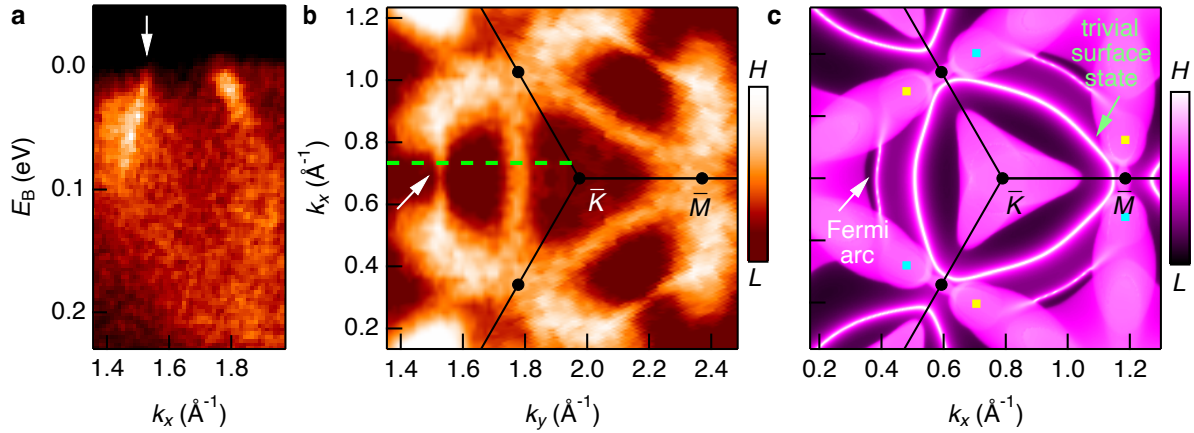
FIG. S9: **Candidate topological Fermi arc.** (a) Energy-momentum ARPES spectrum and (b) ARPES Fermi surface in the vicinity of the $\bar{K}$ point, acquired at $h\nu = 130$ eV, linear horizontal light polarization, $\bar{\Gamma} - \bar{K}$ APRES slit alignment, second through fourth surface Brillouin zones, $T = 20$ K. White arrows indicate a candidate topological Fermi arc. (c) *Ab initio* calculation of the surface density of states at the Fermi energy, Sn termination, with SOC. Weyl point predictions marked by the yellow (positive chirality) and cyan (negative chirality) squares, connected by a Fermi arc and near a closed triangular trivial surface state.
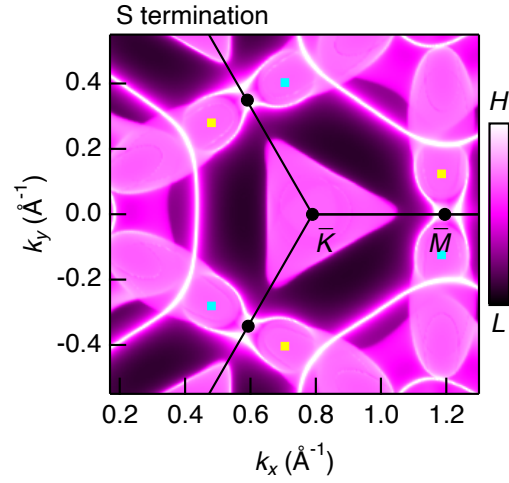
FIG. S10: **Sulfur termination calculation.** *Ab initio* calculation of the surface density of states at the Fermi energy, S termination, including spin-orbit coupling, analogous to Fig. S9c. We observe that our photoemission spectra are best captured by the Sn termination calculation.
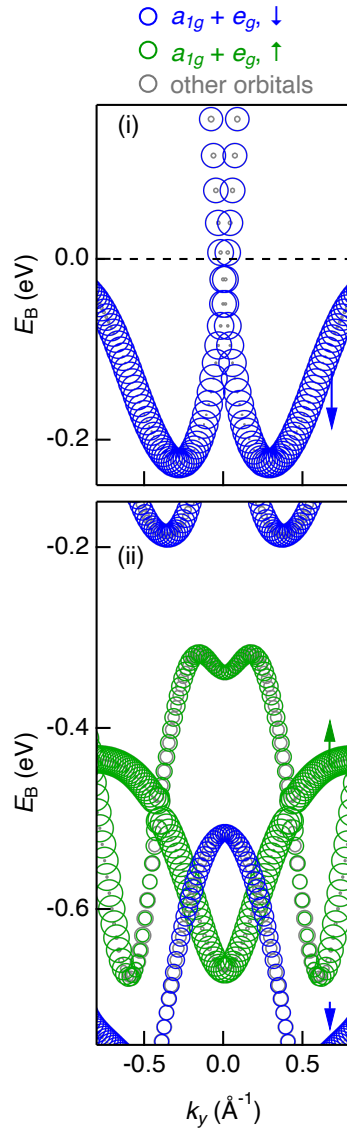
FIG. S11: **Orbital decomposition of the Weyl loop and deep valence bands.** Composition on Cut (i) and Cut (ii), ignoring SOC, under FM order (see Fig. 2). The circles mark the fraction of orbital weight originating from the Co $3d$ a_{1g} and e_g manifolds for up and down spin (green & blue) and all other orbitals (gray). The a_{1g} and e_g manifolds of the D_{3d} point group include d_{z^2}, $d_{x^2-y^2}$ and d_{xy}, which are all heavily hybridized in the present case [62]. The Weyl loops and deep bands exhibit similar orbital composition.